POLITECNICO DI TORINO
Repository ISTITUZIONALE

Design of Ni-coordinated MOF on stainless steel via electrodeposition as efficient and stable oxygen evolution electrode for alkaline water electrolysis

Original
Design of Ni-coordinated MOF on stainless steel via electrodeposition as efficient and stable oxygen evolution electrode for alkaline water electrolysis / Volanti, V.M., Zaffora, A., Iannucci, L., Grassini, S., Inico, E., Saetta, C., Di Liberto, G., Santamaria, M.. - In: ELECTROCHIMICA ACTA. - ISSN 0013-4686. - ELETTRONICO. - 511:(2025), pp. 1-13. [10.1016/j.electacta.2024.145416]

Availability:
This version is available at: 11583/2995165 since: 2024-12-10T15:57:24Z

Publisher:
Elsevier

Published
DOI:10.1016/j.electacta.2024.145416

Terms of use:

This article is made available under terms and conditions as specified in the corresponding bibliographic description in the repository

Publisher copyright

(Article begins on next page)

25 November 2026

Electrochimica Acta 511 (2025) 145416

Contents lists available at ScienceDirect

Electrochimica Acta

journal homepage: www.journals.elsevier.com/electrochimica-acta

Design of Ni-coordinated MOF on stainless steel via electrodeposition as efficient and stable oxygen evolution electrode for alkaline water electrolysis

Valentina Maria Volanti [a], Andrea Zaffora [b,*], Leonardo Iannucci [a], Sabrina Grassini [a], Elisabetta Inico [c], Clara Saetta [c], Giovanni Di Liberto [c], Monica Santamaria [b]

[a] Dipartimento di Scienza Applicata e Tecnologia, Politecnico di Torino, Corso Duca degli Abruzzi 24, Torino 10129, Italy
[b] Dipartimento di Ingegneria, Università degli Studi di Palermo, Viale delle Scienze, Ed. 6, Palermo 90128, Italy
[c] Dipartimento di Scienza dei Materiali, Università degli Studi di Milano Bicocca, Via Roberto Cozzi 55, Milano 20125, Italy

ARTICLE INFO

Keywords:
Metal-organic framework
Oxygen evolution reaction
Stainless steel
Alkaline electrolysis
Ni-based electrocatalyst

ABSTRACT

Ni-succinate/tartrate metal-organic framework (MOF) structures were synthesized on 304 stainless steel (SS) mesh by electrodeposition to prepare porous electrodes for oxygen evolution reaction (OER) in alkaline conditions. Morphological and compositional studies confirmed the synthesis of Ni-coordinated MOF nanoparticles onto the SS mesh. Succinate and tartrate-based MOFs were successfully tested as electrocatalysts for OER in 1 M KOH solution in both batch and flow-through cell configurations, assessing a low Tafel slope value of 46 mV dec^{-1} and overpotential value at 10 mA cm^{-2} of 326 mV. These electrodes further showed high electrocatalytic durability in a 100 h stability test at 50 mA cm^{-2}. The stability test was carried out in both 1 M KOH and in 6 M KOH aqueous solution, being the latter close to the real electrolyte composition of industrial alkaline electrolyzers, proving an outstanding electrocatalytic durability. Theoretical analysis helped in understanding reaction mechanism depending on the nature of the active phase. This study shows a valuable approach for designing platinum group metals (PGMs) and critical raw materials (CRMs)-free electrodes for industrial alkaline water electrolysis.

1. Introduction

The increase in world population and societal innovation is leading to a higher energy demand. Until a few years ago, the main source of energy supply has been fossil fuels. However, their burning has led to the emission of a huge amount of CO_2, air pollution, and climate change. Moreover, they are being exhausted, therefore modern society needs to find new sources of renewable energy. Renewable sources are generally abundant, but they are intermittent, thus a way to store energy from renewable sources is needed.

One of the UN's sustainable development goals (SDGs) is the SDG7, i.e. "ensure access to affordable, reliable, sustainable and modern energy for all" [1]. In this context, exploiting extra renewable energy to produce green hydrogen could be the way to have sustainable and climate-safe energy [2]. Indeed, green hydrogen is going to be essential for those industrial sectors with high energy demand as heavy industry, aviation and international shipping [2,3], that are hard-to-abate. Moreover, green hydrogen can represent the way to produce clean energy through, for instance, fuel cell technology, i.e. an electrochemical cell that converts chemical energy of hydrogen in electricity producing only water and heat, without any by-products or emissions.

Green hydrogen can be produced by electrochemical water splitting, or water electrolysis, i.e. a process where electrical energy is used to electrochemically produce gaseous hydrogen and oxygen, at the cathode and at the anode respectively, from a unique reactant: water [4,5]. Commercial water electrolysis technologies are, to date, proton exchange membrane (PEM) and alkaline electrolyzers [6]. Regardless of the considered water electrolysis technology, a large-scale deployment foresees the usage of highly efficient, durable and low-cost materials.

In a water electrolysis system, the oxygen evolution reaction (OER) at the anode needs a significantly higher overpotential with respect to the cathodic hydrogen evolution reaction (HER), due to its sluggish kinetics and to stability issues of anodic parts (electrocatalyst, bipolar plate) under strong oxidizing conditions [7–9]. Finding highly active,

* Corresponding author.
E-mail address: andrea.zaffora@unipa.it (A. Zaffora).

https://doi.org/10.1016/j.electacta.2024.145416
Received 30 August 2024; Received in revised form 7 November 2024; Accepted 23 November 2024
Available online 24 November 2024
0013-4686/© 2024 The Authors. Published by Elsevier Ltd. This is an open access article under the CC BY-NC-ND license (http://creativecommons.org/licenses/by-nc-nd/4.0/).

durable and low-cost electrocatalysts for OER, thus without the use of platinum group metals (PGMs) and critical raw materials (CRMs), is a significant challenge but crucial to contribute to the worldwide deployment of the technology. Operating in alkaline conditions, the usage of Ir-based electrocatalyst for OER can be avoided and stack components, such as porous transport layers (PTLs) and bipolar plates, can be made with Ni, replacing typical Ti-based parts [2,10].

During the past two decades, metal−organic frameworks (MOFs) have attracted much attention by scientific community because of their peculiar features that make them suitable for many applications, such as catalysis, sensors, gas adsorption or separation, energy storage and so on [11–15]. MOFs are carbon-based materials that also comprise an inorganic part. Indeed, a MOF usually contains a metal cation or a cluster coordinated by an organic ligand [14]. Depending on the synthesis method, many important properties of MOFs can be controlled, such as porosity, functionalities and structure [16–18]. Regarding electrocatalysts application, MOFs have been deeply studied for both HER and OER, and also for oxygen reduction reaction (ORR). In fact, their peculiar nanoscale porosity leads to an enhancement in active sites density, due also to the distribution of metal center at atomic level, and mass transport [17,19–23]. Nevertheless, typically MOFs synthesis requires expensive and, often, toxic organic ligands and it is usually carried out using complex processes that hinder the deployment of these materials at industrial level. In this regard, electrochemical techniques are considered as the best options for an industrial implementation of MOFs synthesis, since they allow the large-scale production both as powder and as thin film or coating [12,24–26] and the optimization of parameters of the electrochemical synthesis can lead to a tailored MOF for specific application.

Here, we report the preparation of MOF-based electrodes for improving OER performance in alkaline conditions, using an industrially relevant deposition technology. This work is in synergy with the goal of a deployment of water electrolysis technology, necessary to produce in large-scale green hydrogen. The latter can be used in the future to produce clean energy through suitable electrochemical power sources, e.g. fuel cells. MOF was the effective electrocatalytic layer and was composed by Ni and a non-toxic and easily available organic ligand, such as succinate [27–30] or tartrate [31–33] anion, derived by the deprotonation of corresponding succinic acid and tartaric acid. In fact, MOF was prepared by cathodic electrodeposition in mild operating conditions, directly on a non-expensive 304 stainless steel (SS) mesh, that worked as substrate of the electrocatalytic layer and could be also employed as porous transport layer in next-generation zero-gap water alkaline electrolyzers. A morphological and compositional analysis of the layers was carried out to verify the successful synthesis through electrodeposition of the MOF layer. Electrochemical characterization was carried out both in 1 M aqueous KOH solution and in 6 M aqueous KOH solution to study the electrocatalytic activity of the electrodes, as well as their stability with a 100 h chronoamperometric test at 50 mA cm^{-2}. The experimental analysis was complemented by atomistic simulations at the level of density functional theory (DFT) to provide some mechanistic understanding of the observed results.

2. Materials and methods

2.1. Electrosynthesis of MOFs

All the investigated electrodes of this study have been prepared by an electrodeposition process. The substrate was a stainless steel (AISI 304) mesh, pretreated with acetone for 5 min and with an aqueous solution 0.5 M of H_2SO_4 for 10 min in ultrasonic bath. Electrodeposition was carried out in a three-electrode cell (see Fig. 1), with two Pt nets acting as counter electrodes to guarantee a uniform deposition onto the substrate, an Ag/AgCl/3.5 M KCl electrode as reference, and the SS mesh as working. Electrodes were immersed in an aqueous solution 8.75 mM of succinic acid ($C_4H_6O_4$, NiSuc sample) or tartaric acid ($C_4H_6O_6$, NiTar sample) and 7.5 mM of $NiCl_2$ (pH = 3). An electrode potential of −1.4 V vs Ag/AgCl was applied, for 15 or 30 min, through a VERSASTAT 3 potentiostat at room temperature.

2.2. Morphological and compositional analysis

Morphology of the MOF electrodes was assessed by using a FEI Quanta 200 FEG Scanning Electron Microscope (SEM) instrument, using EDX (X-ray energy dispersive system) to have information about the composition of the catalytic layers.

X-ray diffraction (XRD) patterns were recorded using a PANalytical Empyrean diffractometer equipped with a PIXcel1D (tm) detector using the CuKα radiation (λ = 0.15405 nm), operating at 40 kV and 40 mA.

Fourier-transform infrared spectra (FTIR) were recorded at room

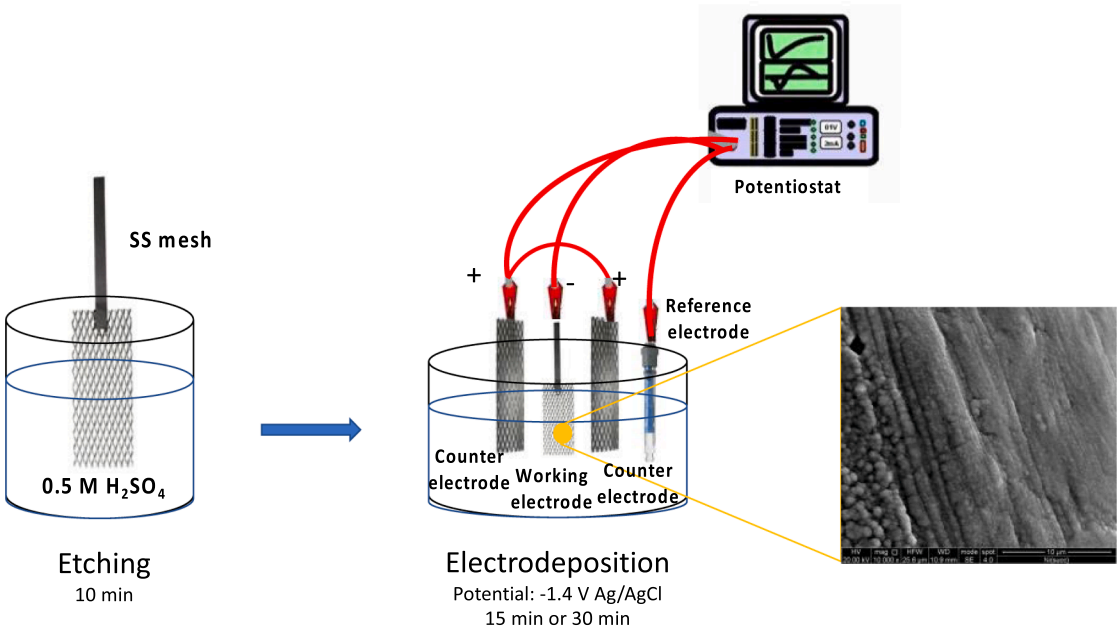

Fig. 1. Sketch of the preparation process of MOF electrodes.

temperature, to study the presence of specific functional groups. Measurements were carried out with a Perkin-Elmer FT-IR/NIR Spectrum 400 spectrophotometer, using the wavenumber range from 4000 to 400 cm^{-1}.

2.3. Electrochemical measurements

Electrochemical measurements were performed in a batch system and in a flow-through (FT) cell (see Figure S1a and S1b, respectively), using a PARSTAT 2263, with a three-electrode configuration.

The electrolyte was an aqueous solution of 1 M KOH, the counter electrode was a dimensionally stable anode mesh (DSA) while a Hg/HgO/1 M NaOH was employed as reference. All the electrode potentials measured vs Hg/HgO were then referred to the Reversible Hydrogen Electrode (RHE) to have a direct comparison with data reported in literature, according to the equation:

$$E_{RHE} = E_{Hg/HgO} + 0.1\ V + 0.059\ pH \quad (1)$$

Electrochemical active surface area (ECSA) was evaluated by means of the double layer capacitance value, estimated in an inert atmosphere (Ar-saturated), to avoid oxygen reduction, in an aqueous solution 0.1 M of ammonium biborate (pH ≈ 9). This investigation was performed by two methods: recording cyclic voltammetries (CVs) in a range of potential avoiding any faradaic process, or through EIS spectra recorded at 0.1 V RHE, using an a.c. signal amplitude of 10 mV with frequencies 0.1–10^5 Hz through the PARSTAT 2263. The recorded impedance spectra were then modeled by ZSimpWin with a suitable equivalent electric circuit. EIS spectra were also collected at the electrode potentials of 1.52 V RHE and 1.68 V RHE, in 1 M KOH electrolyte, to study the electrocatalytic activity of the electrodes. To have information about electrocatalysts performances, i.e. overpotential values, Tafel slope values, potentiodynamic (Linear Sweep Voltammetries, LSVs) tests were carried out at 10 mV s^{-1}, starting from 0.9 V RHE. Reported results have been already corrected considering a 95 % iR compensation.

The stability of the electrocatalysts was evaluated by galvanostatic measurement at 50 mA cm^{-2} for 100 h in 1 M KOH and 6 M KOH.

2.4. Computational details

Spin polarized DFT calculations were performed with the VASP code [34–36] using the generalized gradient approximation, as implemented in the PBE functional [37]. The following valence electrons were treated explicitly: H (1s), C (2s, 2p), O (2s, 2p) and Ni (5s, 4d). They have been expanded on a set of plane waves with a kinetic energy cutoff of 400 eV, whereas the core electrons were treated with the Projector Augmented Wave approach (PAW) [38,39]. The threshold criteria for electronic and ionic loops were set to 10^{-4} eV and 10^{-2} eV/Å, respectively. The sampling of the reciprocal space was restricted to the gamma point, because of the cell dimensions. Dispersion forces have been included according to the Grimme's D3 parametrization [40]. Single point PBE0 [41,42] calculations have been performed to refine the electronic structure [43]. This is typically a reasonable choice to provide accurate results without the need of performing computationally demanding geometry optimizations with hybrid functionals. Previous results suggested the importance of adopting self-interaction corrected functionals when modeling SACs [44–46]. We considered a molecular model where the metal atom is coordinated by two succinate/tartrate ions. We added a vacuum layer of 15 Å to avoid spurious effects due to interaction between periodic replica of the system.

The Gibbs energies were evaluated by adopting the ab-initio thermodynamic approach [47,48], by adding to the DFT energy the contribution of zero-point energy correction and entropy terms. The first were calculated in a harmonic fashion. Entropies of gas phase species were taken from the international tables, and the vibrational entropy of solid-state species was determined through the formalism of the partition function.

3. Results and discussion

3.1. MOF electrodeposition

Electrocatalysts were prepared through an electrodeposition process in aqueous medium containing a Ni-based salt and an organic acid, i.e. succinic or tartaric. Electrodeposition conditions are reported in Section 2.1. Corresponding current density vs time curves are shown in Figures S2a)-d). At that electrode potential and pH conditions, from a thermodynamic point of view, following reactions can occur [49]:

$$½O_2 + 2H^+ + 2e^- \rightarrow H_2O \qquad E_{eq} = 1.05\ V\ SHE \quad (2)$$

$$2H^+ + 2e^- \rightarrow H_2 \qquad E_{eq} = -0.18\ V\ SHE \quad (3)$$

$$Ni^{2+} + 2e^- \rightarrow Ni \qquad E_{eq} = -0.31\ V\ SHE \quad (4)$$

In electrodeposition operating conditions, highest overpotential value can be estimated for reaction (2) (i.e., oxygen reduction reaction) but its contribution to the total circulating current is quite low since this reaction is in limiting current conditions, because of the low O_2 concentration (i.e. its solubility in water at room temperature) and stagnant hydrodynamics condition [50,51]. Reaction (3) overpotential was higher than that of reaction (4) and, as confirmed by visual inspection during the electrodeposition process, hydrogen evolution reaction occurred with consequent local alkalinization near the cathode. If we consider dissociation equilibria of the organic acids due to the presence of hydroxyl and carboxyl groups (see Figures S3a) and S3b)), local alkalinization during electrodeposition process shifts the dissociation equilibrium toward the formation of succinate/tartrate anions. These ions react with metallic cations (Ni^{2+} in our case) leading to the formation of the MOF structure with the succinate/tartrate ions that coordinated Ni^{2+} ions [26,52]. In particular, suc^{2-} or tar^{2-} ligand is chelated to two Ni^{2+} centers, with each Ni^{2+}center coordinated by four oxygen atoms therefore presenting an octahedral coordination geometry. Anyway, possible formation of metallic Ni during the electrodeposition cannot be totally excluded (see below), as reported for other cathodically electrodeposited MOF structures [12].

3.2. MOF-based electrocatalysts morphology and composition

To get information about MOF morphologies, an investigation with SEM microscope was carried out and the results are shown in Fig. 2a)-d) for NiSuc-15 and NiSuc-30 samples (i.e. deposited using succinic acid for 15 and 30 min respectively) and in Fig. 2e)-h) for NiTar-15 and NiTar-30 (i.e. deposited using tartaric acid for 15 and 30 min respectively) samples, respectively.

The comparison of Fig. 2b) and 2d) reveals the effect of deposition time on the morphology of the coating on the SS 304 mesh substrate prepared by using succinic acid. In both cases coatings are composed by particles but, whilst with a 15 min deposition, particles have diameters of 1.1 ± 0.4 μm (see Fig. 2b)), a 30 min deposition leads to a more compact coating composed by particles with lower average diameter, i.e. 0.3 ± 0.1 μm (see Fig. 2d)). Latter morphology is similar to that observed for the coating prepared by using tartaric acid for 15 min (see Fig. 2f)), whilst MOF structure obtained with the same organic acid with 30 min as deposition time has an even more compact morphology (see Fig. 2h)), being difficult to distinguish nanoparticles. In Table 1 the results of EDX investigation are reported, listing the at.% of C, O, Cr, Fe and Ni.

Detected Fe and Cr can be ascribed to the 304 SS substrate whilst C, O and Ni presence are related to the coating presence, although Ni is also present in the substrate. C presence is directly related to the succinate/tartrate proving the deposition of a MOF-like structure. Regarding NiTar-15 sample, higher Fe and Cr contents were detected, probably due

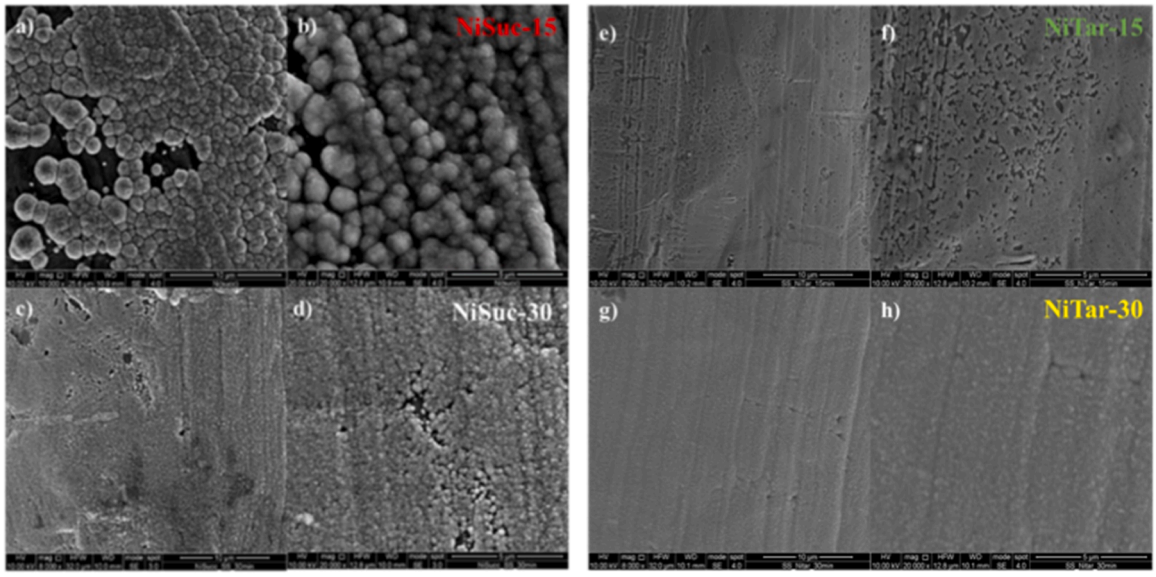

Fig. 2. SEM images of NiSuc-15 sample at a) 10000x and b) 20000x magnification. SEM images of NiSuc-30 sample at c) 8000x and d) 20000x magnification. SEM images of NiTar-15 sample at e) 8000x and f) 20000x magnification. SEM images of NiTar-30 sample at g) 8000x and h) 20000x magnification.

Table 1
Atomic composition of 304 mesh sample and all the electrodeposited MOF structures obtained by EDX.

Sample	C [at%]	O [at%]	Cr [at%]	Fe [at%]	Ni [at%]
304 mesh		10.86	17.97	63.45	7.72
NiSuc-15	17.85	5.16	2.48	7.23	67.28
NiSuc-30	22.99	7.31	2.82	8.30	58.58
NiTar-15	33.19	16.28	9.23	31.19	10.11
NiTar-30	25.1	6.35	2.52	7.7	58.34

to the lower coverage degree of the MOF coating and, therefore, a higher signal from the SS substrate was collected.

Hydrophilicity of MOF-based coatings was also assessed by measuring water contact angle, that is ~ 80° (see Fig. 3a) and 3b)), for both succinate and tartrate-containing layers.

XRD patterns of NiSuc-15 and NiTar-15 samples are reported in Fig. 3d). In this case, to have better resolution, MOF structures were deposited on a glass/FTO sample, therefore several peaks of the diffractogram are related to FTO. Crystal structure features do not change with the deposition time, regardless of the organic acid used during the electrodeposition process. Diffraction peak at 44.5°, 51.86° and 76.39° can be assigned respectively to the (111), (200) and (220) planes of face-centered cubic (FCC) metallic Ni [53,54]. As can be noticed, other

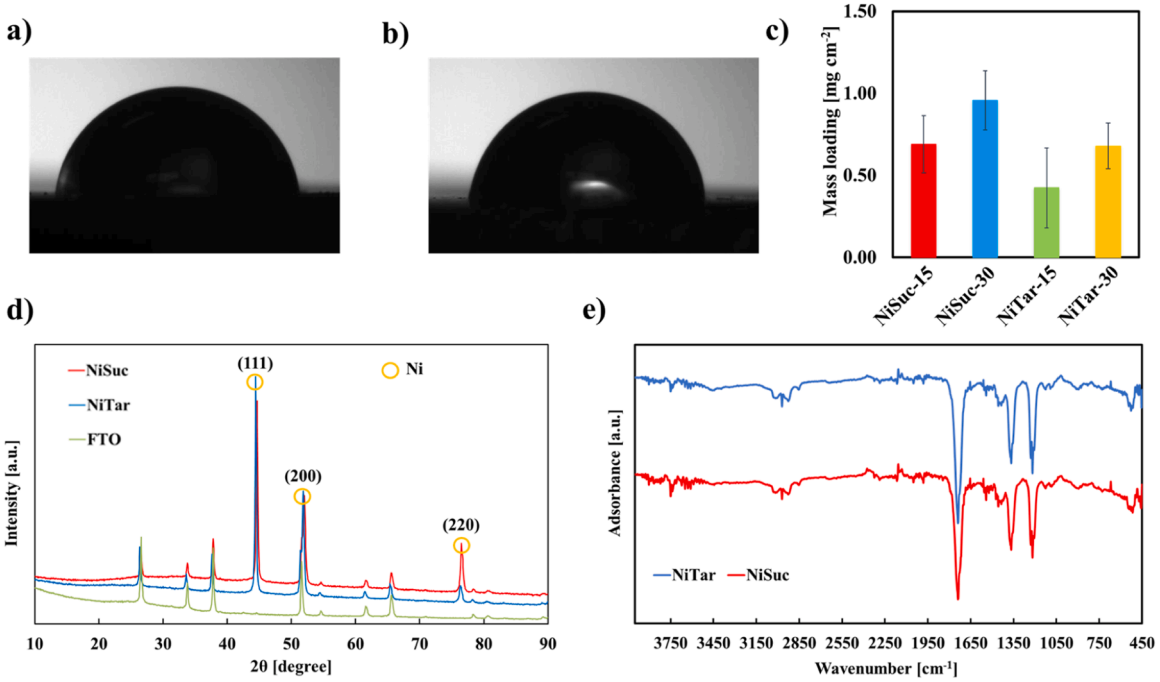

Fig. 3. Static water contact angle for a) NiSuc-30 and b) NiTar-30 samples. c) Mass loadings for all the investigated MOF electrodes. d) XRD patterns of NiSuc-15, NiTar-15 and FTO samples. e) FTIR spectra of NiSuc-30 and NiTar-30 samples.

diffraction peaks can be attributed to the FTO substrate. This result can be explained by considering the possible electrodeposition of metallic Ni during the preparation of the electrocatalysts since the electrode potential during the electrodeposition is more cathodic than equilibrium potential related to the Ni/Ni^{2+} redox couple (see eq. (3)).

FTIR spectra of NiSuc-30 and NiTar-30 samples are shown in Fig. 3e). Bands at 1399 cm^{-1} and 1125 cm^{-1} can be attributed to (C—H). The vibration of the carboxylate group ν(C—OO^-), coordinated with Ni^{2+}, is observed at 1367 and 1542 cm^{-1}. The ν(C—C) stretching, appears at 1081 cm^{-1}, whilst the vibration at 1450 cm^{-1} corresponds to (C—OH). The broadband with maxima at 2971 cm^{-1} comes from the (O–H) stretching vibrations of water ligands, meaning the presence of hydrogen bonding in the complex [55–57]. We also recorded FTIR spectra for pure succinic acid and tartaric acid (see Figure S4). In the case of succinic acid, the stretching frequency of carboxylic groups in free succinic acid appears at 1681 cm^{-1} but it disappears in the electrodeposited sample (see Fig. 3e), assessing the complexation of Ni by succinate groups [56]. In the case of tartaric acid, the peak at 3399 cm^{-1} can be related to the presence of O–H stretching in the carboxyl group [58], whose disappears in the case of electrodeposited sample due to the complexation of Ni by carboxyl groups of tartrate ions. FTIR features do not change with the electrodeposition time.

3.3. OER electrochemical performance

To evaluate the electrocatalytic performance of MOF-based electrodes, electrochemical measurements have been carried out, in particular, Electrochemical Impedance Spectroscopy (EIS) measurements. It is noteworthy to underline that electrochemical measurements have been carried out in two different configurations: batch and flow-through (see Figures S1a and S1b). These tests allowed to understand if catalytic layers can properly work also in flow through conditions, i.e. mimicking the use of this coating in a porous transport layer in an industrial electrolyzer configuration. Potentiodynamic tests carried out in 1 M KOH relating to all the investigated electrodes, in batch and in flow-through configuration, are shown in Fig. 4a) and 4c) whilst corresponding Tafel plots are shown in Fig. 4b) and 4d).

A first relevant information arising from the current density vs potential curves is that the MOF coating can completely hinder the onset of transpassive dissolution due to chromate formation even under a very positive potential. Indeed, thanks to the passivating action of the presence of the MOF, there are not current peaks associated to Cr(III)

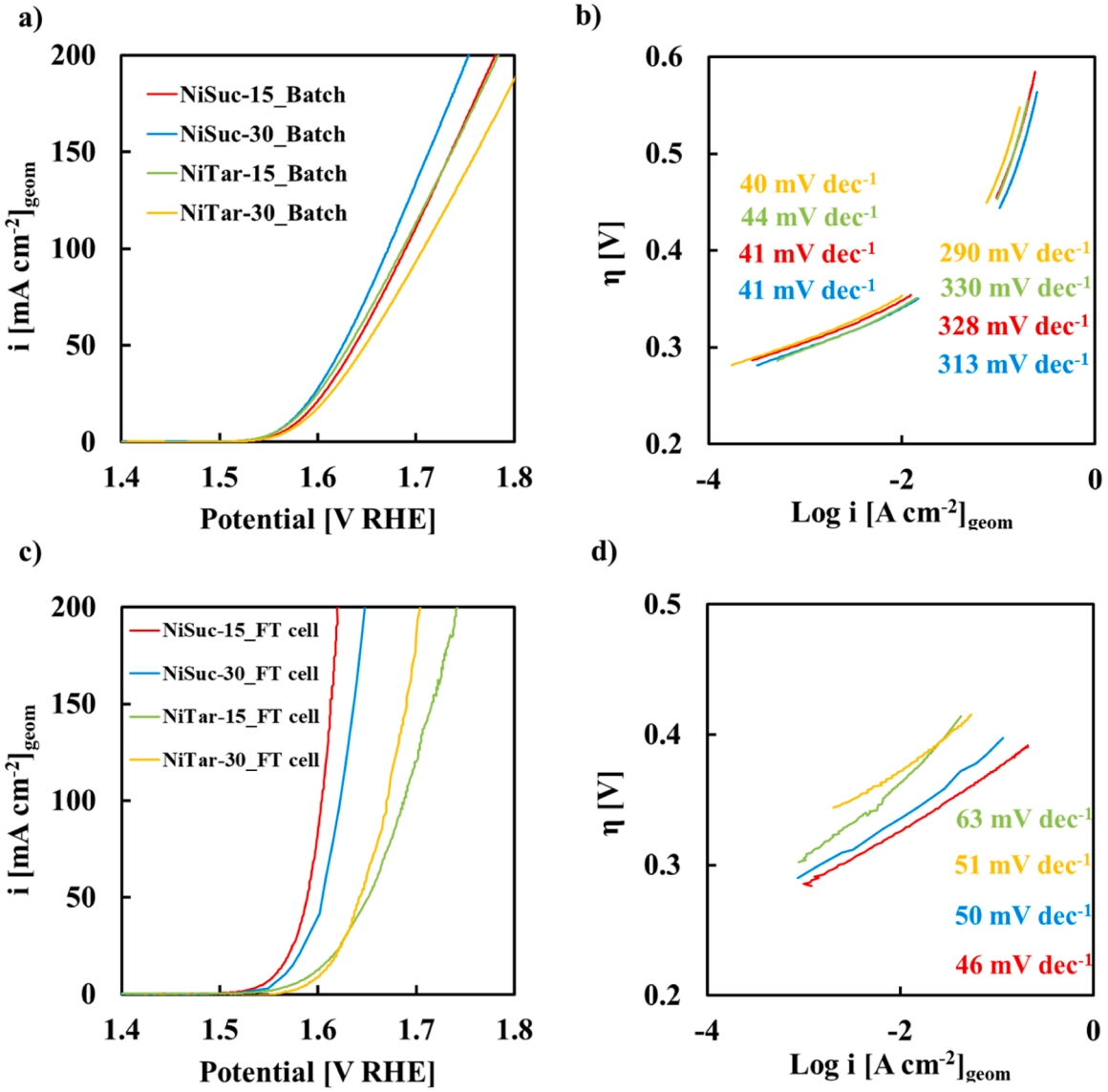

Fig. 4. Comparison of i vs. potential curves, related to all the investigated electrodes, carried out in a) batch and c) flow through configurations. b) Tafel plot extrapolated from Fig. 4a) and d) Tafel plot extrapolated from Fig. 4c).

oxidation [59].

As it is possible to notice from Fig. 4a), in batch configuration, MOF electrodes' performances are very close. In fact, the onset electrode potential for OER has the same value for all the electrodes, 1.5 V RHE that leads to an onset overpotential value, η_{onset}, of 270 mV. Another important performance indicator is the overpotential value measured at 10 mA cm^{-2}, η_{10}, because this current density value is considered as the operating current density of a device that converts solar energy to hydrogen [60]. The latter is comprised between 340 mV and 352 mV for the characterization carried out in batch system. These values are comparable with those reported in literature for MOF-based electrocatalysts [21] but, in our case, the electrocatalyst has been synthesized with a full electrochemical process, which can be easily scaled at industrial level, using organic molecules that can be easily handled with no further toxicity issues, and using a cheaper 304 SS substrate with respect to typical more expensive Ni foams. This result is also significant by looking at the mass loadings (reported in Fig. 3c)) that are in the range between 0.42 ± 0.1 and 0.96 ± 0.1 mg cm^{-2}, i.e. lower than those typically reported for MOF-based electrocatalysts [21], indicating an enhanced mass activity of our succinate and tartrate-based electrocatalysts.

An important factor to evaluate electrocatalytic performances of the electrodes is the slope of the so-called Tafel line, that has the following equation:

$$\eta = a + b\ log(i) \tag{5}$$

where η is the overpotential and i is the current density. Being Tafel line an approximation of the most general Butler-Volmer equation, *a* parameter directly depends on the exchange current density, i_0, and *b* is called Tafel slope. The lower is the latter, less overpotential is needed to drive oxygen evolution reaction. Moreover, Tafel slope value can be associated to the peculiar reaction mechanism of OER for a specific electrode, since a characteristic Tafel slope value can be correlated to the rate determining step (RDS) of the overall OER, that in turn is typically considered as composed by 4 different reaction steps [61–63]. Comparing Tafel slope values reported in Fig. 4b), it is noteworthy to mention that, in low current density range, low Tafel slope values are extracted (i.e. between 40 and 44 mV dec^{-1}), regardless on the composition of MOF electrocatalytic layer, in agreement with charge transfer-controlled reaction mechanism. When current density increases, up to about 200 mA cm^{-2}, Tafel slope increases to almost 300 mV dec^{-1}, demonstrating that reaction is controlled by "non-kinetic" effects, related to the formation of oxygen bubbles and, therefore, to mass transfer issues [64].

Considering the electrochemical performance in flow-through configuration (see Fig. 4c), succinate-based MOF electrodes performed better with respect to tartrate-based ones, not in terms of η_{onset}, that is similar for all the electrodes, but more in terms of Tafel slope values, which depend on the composition of the electrocatalytic layer (i.e. between 46 for NiSuc-15 sample and 63 mV dec^{-1} for NiTar-15 sample). This cell configuration plays a crucial role in bubbles management, helping produced oxygen in detaching from the electrode indicating a more efficient reaction mechanism. Nevertheless, it can also provoke additional mechanical stresses to catalytic layer that needs to be tested with a long-lasting measurement (see below). Anyway, it is interesting to notice that Tafel slope value is constant up to 200 mA cm^{-2}, in the case of NiSuc-15 and NiSuc-30 samples, and it starts to increase in the case of NiTar-15 and NiTar-30 samples, assessing that also MOF composition and thickness have a direct influence on oxygen evolution reaction mechanism. With lower Tafel slope values, also η_{10} values decreased reaching 326 mV and 336 mV for NiSuc-15 and NiSuc-30 samples, respectively. Moreover, lowest Tafel slope value, i.e. 46 mV dec^{-1}, is close to that estimated for benchmark electrocatalysts for OER, as IrO_2 and RuO_2 [65,66], and equal to that estimated for another full electrochemical MOF-based electrocatalyst, synthesized by Wang et al. [67] that is considered as one of the best performances reported in literature for electrochemically prepared MOF for electrocatalytic purposes [12].

Impedance spectra were recorded in FT configuration at two different electrode potential values, i.e. 1.52 V RHE and 1.67 V RHE. Spectra are reported in Fig. 5a) and 5b) in Nyquist representation.

To get information from EIS spectra, a suitable equivalent electrical circuit (EEC) is needed to model the electrochemical behavior of the system working at those specific working electrode potential values. EEC used to fit impedance spectra in the case of MOF electrodes comprises a series between R_s, that is the solution resistance, and a parallel between R_{CT}, the charge transfer resistance, and Q_{DL}, used to model the non-ideal electrical double layer capacitance through a so-called constant phase element. Fitting parameters are reported in Table 2.

At 1.52 V RHE the reaction is still not well activated, as evident from the R_{CT} values. These values decrease at 1.67 V RHE and, in particular, it is noteworthy to mention that lowest R_{CT} values are reported for NiSuc-15 and NiSuc-30 samples, in agreement with results reported in Fig. 4c).

For a correct evaluation of electrocatalytic activity of the MOF-based electrodes, the measurement of the electrochemical active surface area (ECSA) is crucial since a high ECSA reflects a higher number of active sites, leading to enhanced performances. The evaluation of the electrode double layer capacitance, C_{DL}, was used to have information about ECSA. At this aim, EIS spectra were recorded in 0.1 M ABE, in an inert atmosphere (i.e. Ar-saturated), at 0.1 V RHE, measuring in this way a current due only to non-faradaic processes, thus excluding the contribution due to oxygen reduction reaction. Nyquist plot of spectra recorded for all the samples are reported in Fig. 5d, in comparison with non-deposited 304 SS mesh sample and corresponding fitting parameters are reported in Table S1. C_{DL} values can be obtained from Q_{DL} through the equation [68]:

$$C_{DL} = {Q_{DL}}^{\frac{1}{n}} {R_s}^{\frac{1-n}{n}} \tag{6}$$

From the fitting parameters reported in Table S1 it is possible to notice no significant increase C_{DL} values after the electrodeposition process, which can be attributed to the similar roughness (therefore active area) of the deposited MOF structures with respect to the bare 304 SS mesh. R_{CT} value reported for the 304 SS mesh sample is quite high (3×10^4 Ω cm^2) as typical for an ideally polarizable interface, and its order of magnitude is the same as the one obtained for electrodeposited MOFs. These high R_{CT} values result from the fact that no Faradaic process can occur at this potential in these operating conditions. C_{DL} value can be also calculated also by means of cyclic voltammetries (CVs) recorded at several scan rates, in a potential range where there is no response due to faradaic currents (e.g. between 0.1 RHE and 0.42 RHE). CVs are reported for all the investigated electrodes in Figures S5a), S5c), S5e) and S5 g). Double-layer capacitive current, i_{CL} can be correlated to scan rate, v, and C_{DL} according to the relationship $i_{CL} = C_{DL}\ \nu$ [69], and therefore, C_{DL} can be also derived from the slope of the i_{CL} vs. ν plot. C_{DL} values estimated through both methods are very close, proving the reliability of obtained C_{DL} values. Knowing C_{DL} values, the roughness factor *r* can be estimated through Eq. (7)):

$$r = \frac{C_{DL}}{50\ \mu F\ cm^{-2}} \tag{7}$$

considering that a C_{DL} value of 50 μF cm^{-2} was estimated for a mirror-finished AISI 304 sample [70]. *r* values, estimated as average between the two reported methods, are then reported in Table 3.

From estimated *r* values, and from what assessed by looking at the electrodes' morphology by SEM (see Figs. 1 and 2), the ECSA is very close to the area of the bare 304 SS mesh sample. Furthermore, it is possible to obtain specific surface area (SSA) values for the MOF structures knowing catalyst mass loadings (see Fig. 3c)). SSA values range between 0.27 ± 0.08 $m^2\ g^{-1}$ for NiSuc-15 sample and 0.52 ± 0.26 $m^2\ g^{-1}$ for NiTar-15 sample.

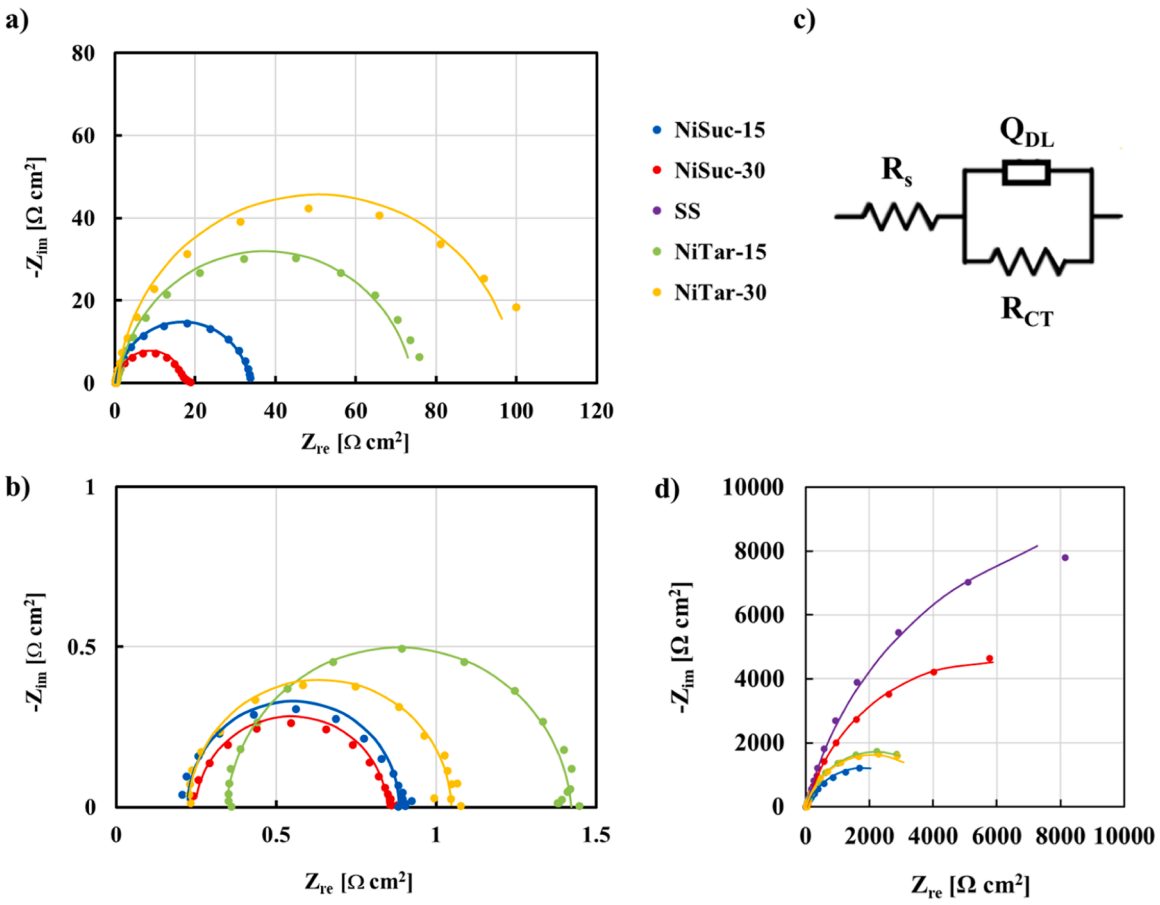

Fig. 5. Electrochemical impedance spectra recorded at a) 1.52 V RHE and b) 1.67 V RHE for all the investigated electrodes. c) Equivalent electrical circuit used for fitting procedure. d) Nyquist plot of impedance spectra recorded for the evaluation of ECSA of all the electrodes. Fitting data are those reported with continuous lines.

Table 2
Fitting parameters of EIS spectra recorded at 1.52 V RHE and 1.67 V RHE related to all the electrodes in FT configuration.

Sample	V [V RHE]	R_s [Ω cm²]	R_{CT} [Ω cm²]	Q_{DL} [S s^n cm^{-2}]	n	χ^2
NiSuc-15	1.52	0.20	17	2.1×10^{-3}	0.95	6.5×10^{-2}
	1.67	0.25	0.6	1.1×10^{-3}	0.96	3.6×10^{-2}
NiSuc-30	1.52	0.17	34	2.1×10^{-3}	0.92	3.2×10^{-2}
	1.67	0.22	0.7	7.5×10^{-4}	1	1.2×10^{-2}
NiTar-15	1.52	0.64	74	1.8×10^{-3}	0.90	1.4×10^{-1}
	1.67	0.34	1.1	8.4×10^{-3}	0.95	3.1×10^{-4}
NiTar-30	1.52	0.64	100	1.7×10^{-3}	0.94	2.7×10^{-2}
	1.67	0.23	0.8	6.7×10^{-4}	0.98	1.1×10^{-3}

Table 3
Roughness factor of all MOF structures investigated in this study.

	304 SS mesh	NiSuc-15	NiSuc-30	NiTar-15	NiTar-30
Roughness factor r	1.40 ± 0.3	1.90 ± 0.4	1.05 ± 0.05	1.8 ± 0.1	1.8 ± 0.3

3.4. Electrode durability

Another crucial feature for large-scale applications is the stability and durability of the electrodes that can be assessed with a chronopotentiometric test, that we carried out under very stressing and oxidizing conditions, i.e. at 0.05 A cm^{-2} in aqueous 1 M KOH solution, for 100 h. These working conditions chosen for the durability test outperform most of the working conditions reported in literature in terms of current density [71] and stability test time [72] for MOF structures. This stability test was performed for the best electrodes, i.e. NiSuc-15 and Ni-Suc-30 samples, in FT configuration and relating results are shown in Figs. 6a) and b).

Overpotential value for OER remains quite stable for (at least) 100 h, with a value of 435 mV ± 6 mV for NiSuc-15 sample (see Fig. 6a) and 459 ± 16 mV for NiSuc-30 sample (see Fig. 6b), demonstrating the high stability of both electrodes. Moreover, no material detachment from the electrodes was assessed by SEM images of both samples after durability test (see Figure S6).

To further test the stability of electrochemically prepared MOF electrodes, we also carried out electrochemical measurements in 6 M KOH aqueous solution, i.e. electrolyte concentration that is actually used at industrial level in alkaline water electrolyzers. LSV measurements performed in these operating conditions for NiSuc-30 sample, both in batch and in FT cell configurations, are shown in Fig. 7a) with corresponding Tafel plot in Fig. 7b).

It is noteworthy to mention that also in this highly alkaline environment there is no evidence of transpassive dissolution, and η_{onset} is lower with respect to LSV measured in 1 M KOH solution, i.e. η_{onset} = 210 mV, whilst the Tafel slope value is almost unchanged. This result agrees with the effect of OH^- concentration on the kinetics of the reaction, in particular on the i_0 value. In fact, i_0 can be generally expressed according to the equation [73]:

$$i_0 = Fk^0 {C^*_O}^{(1-\alpha)} {C^*_R}^{\alpha} \quad (8)$$

where α is the transfer coefficient, k^0 is the standard rate constant and C^*_O and C^*_R are the concentration of reactant species/reaction

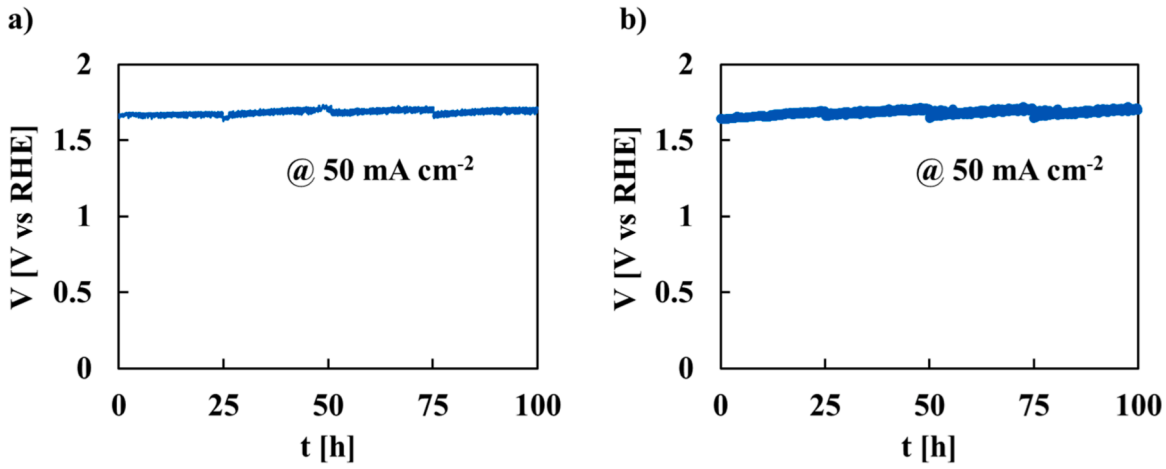

Fig. 6. Durability test carried out at 0.05 A cm^{-2} in aqueous 1 M KOH solution for a) NiSuc-15 and b) NiSuc-30 samples.

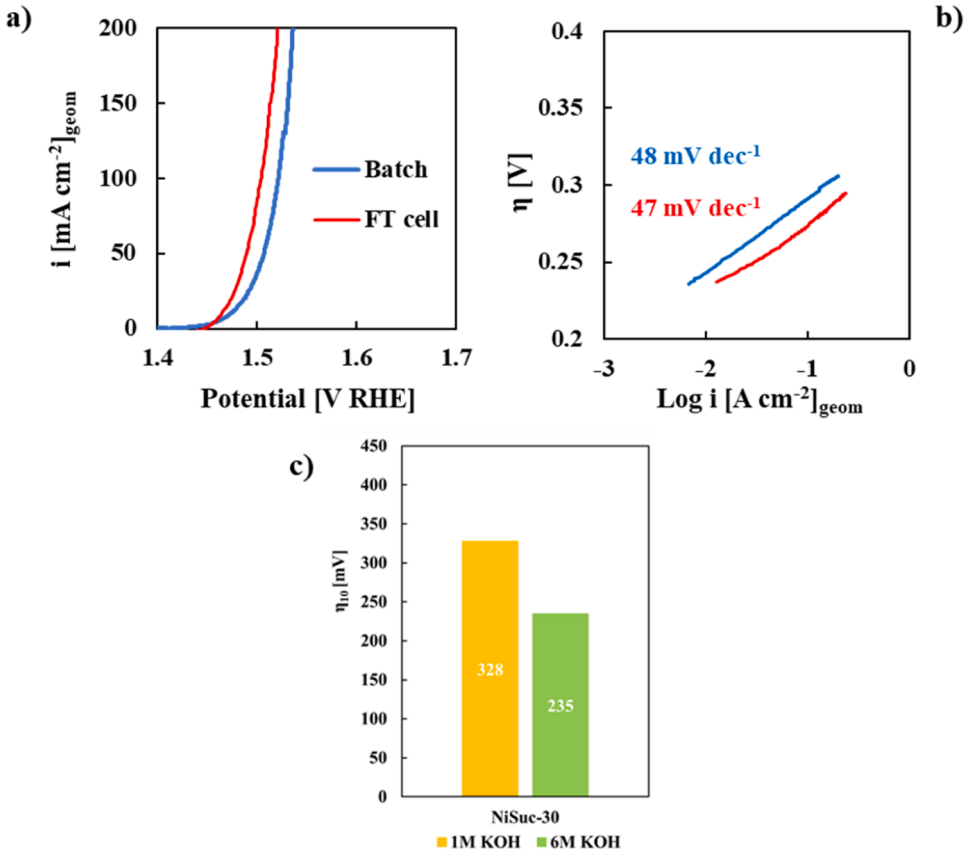

Fig. 7. a) i vs. potential curves recorded in 6 M KOH aqueous solution in batch and FT configuration related to NiSuc-30 sample. b) Tafel plot related to curves shown in Fig. 7a) with corresponding slope values. c) Overpotential values estimated at 10 mA cm^{-2} in 1 M KOH and 6 M KOH aqueous solutions.

intermediates at the electrode/electrolyte interface, considering a generic equilibrium $O + e^- \leftrightarrow R$, representing the latter the RDS of a multistep reaction, as OER is. Consequently, also η_{10} measured in 6 M KOH is lower than that measured in 1 M KOH (see Fig. 7c).

In these operating conditions, it is extremely important to test the stability of the electrodes in terms of electrocatalytic activity, because of possible dissolution phenomena that can be involved at such a high pH value. To assess the durability, we carried out the same stability test, i.e. 100 h at 0.05 A cm^{-2}, but in 6 M KOH solution. The electrode potential vs time curve is reported in Fig. 8a).

As it is possible to note, electrode potential is very stable throughout the 100 h test, at $\eta = 260$ mV, indicating the outstanding stability of this succinate-based MOF electrode from electrocatalytic point of view. Also, the morphology of the catalytic layer is preserved after 100 h stability test, as shown in Fig. 8b), as well as its atomic composition (see Table S2) is very close to that reported soon after the electrodeposition process (see Table 1).

3.5. Computational results

To provide an atomistic description of the OER reaction on NiSuc and NiTar we performed DFT calculations. We modeled Ni single atoms

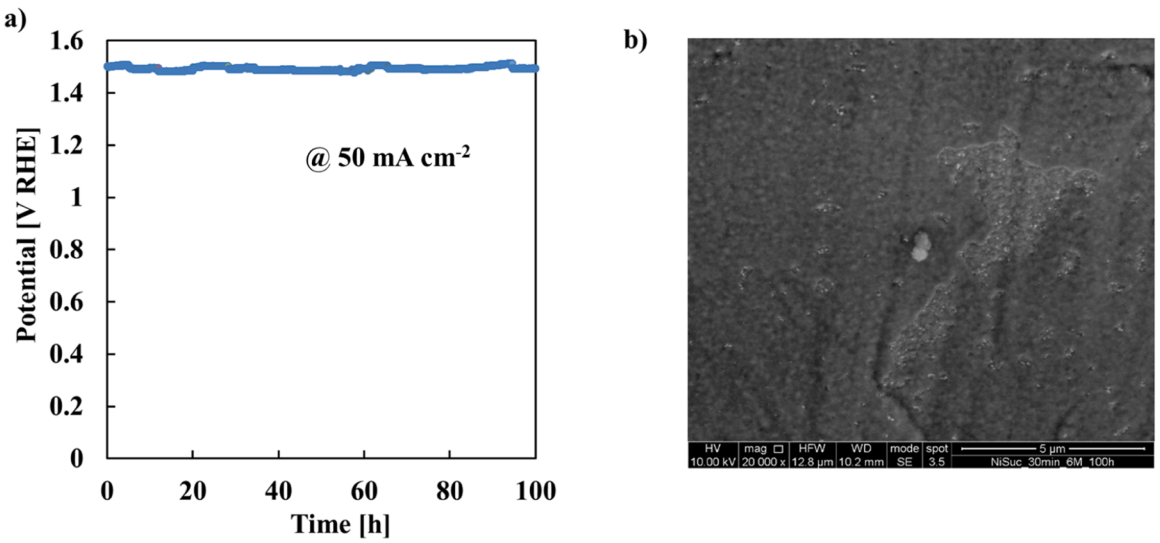

Fig. 8. a) Durability test carried out at 0.05 A cm^{-2}, in 6 M KOH for NiSuc-30 sample. b) SEM micrograph of NiSuc-30 sample after durability test.

having a +II oxidation state. The coordination of the SAC is saturated by the chelate action of two succinate or tartrate ions. For each system two possible configurations of the active phase were found and are shown in Fig. 9 for both systems.

In one case, the coordination of the Ni metal center is square planar (see Fig. 9a) and 9c)), according to the well-known rules of inorganic chemistry, Ni(II) with a d^8 shell. Another possible structure is represented in Fig. 9b) and 9d), where the symmetry of the catalytic site is lower. Interestingly, in the case of NiSuc both structures are possible, as their relative energy is similar, i.e. $\Delta E = 0.25$ eV. In the case of NiTar the square planar configuration is significantly more stable by 1.0 eV, making the formation of the asymmetric conformer unlikely. It must be mentioned that the simulated models contain an extra degree of flexibility as no constrains due to periodic boundary conditions are imposed. However, this is expected to make further unlikely flexible configurations.

OER was modeled by considering the classical reaction path occurring via the formation of classical OH*, O*, OOH* intermediates. At the same time, we also considered the formation of OER unconventional intermediates that have been suggested to form on single-site catalysts [74–76]. Fig. 10 shows all the possible reaction profiles, indicating the number of competing species that can form.

Starting from NiSuc sample, we see that the reaction should go via the classical path but before O_2 release, an oxygen complex forms. The calculated overpotential (η) is rather high, $\eta = 1.11$ V, indicating that the SAC is poorly active (see Fig. 10a). Then, we considered the second SAC model, where the symmetry of the active site is lower. The reaction path is the same of the previous model (see Fig. 10b) but with a smaller overpotential, $\eta = 0.44$ V. Therefore, the lower coordination of the metal center implies a stronger reactivity.

Previous works have suggested that, with single-site catalysts, water is not only the solvent of the reaction, as it can act as a ligand, competing

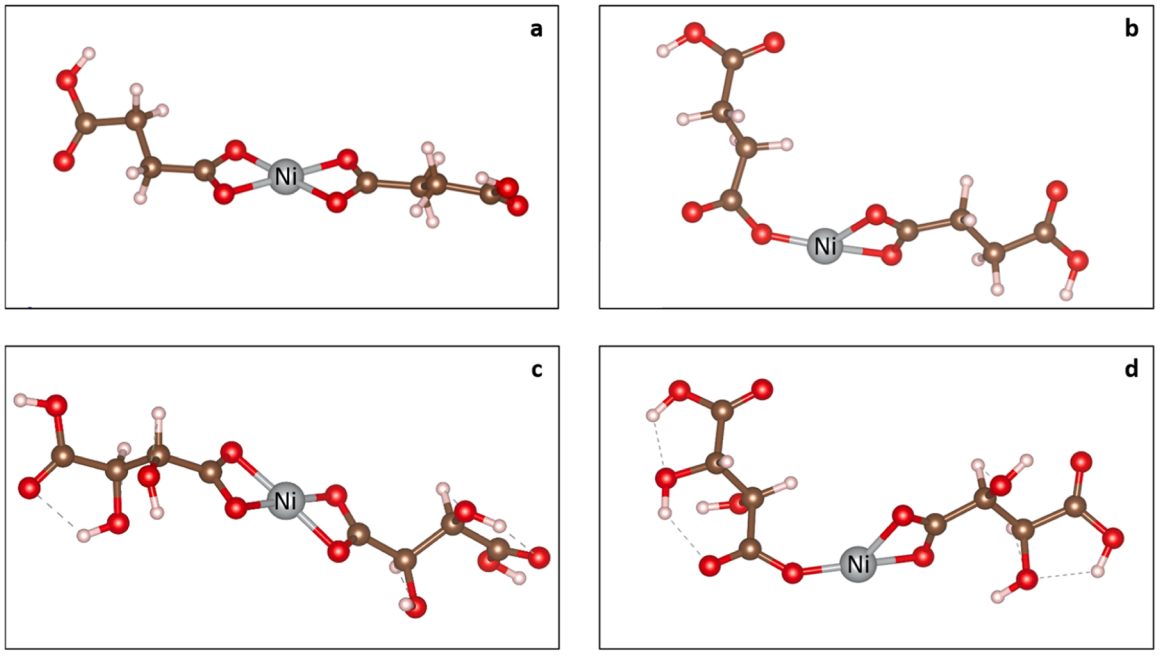

Fig. 9. Structures of a,b) NiSuc and c,d) NiTar samples. Panels a) and c) rely to the square planar coordination of Ni. Panels b) and d) are for asymmetric coordination of Ni.

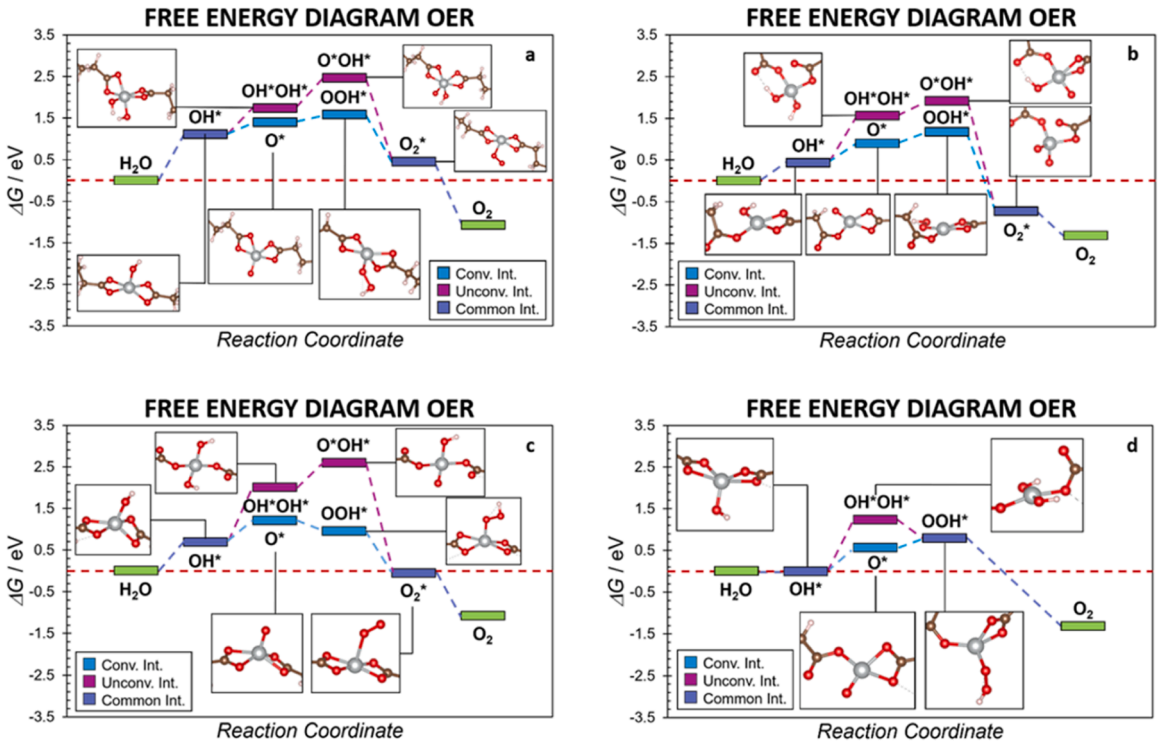

Fig. 10. Calculated OER Gibbs free energy profiles of a,b) NiSuc and c,d) NiTar samples. Panels a) and c) rely to the square planar coordination of Ni. Panels b) and d) are for asymmetric coordination of Ni.

with the reaction intermediates [77,78]. This directly impacts the stability of the intermediates, and the efficiency of the process. We considered the NiSuc catalyst coordinated by one water molecule, in a square pyramidal configuration (see Fig. 11a)).

In this case, some OER intermediates are not stable, indicating that OER is possible on this catalyst only if one assumes to have a naked SAC (see Figs. 10a) and 10c)). If we consider the reaction with less symmetric configuration of the NiSuc catalyst, the OER is also possible by considering the presence of one water molecule coordinating the metal center (see Fig. 11a). The simultaneous presence of two water molecule was

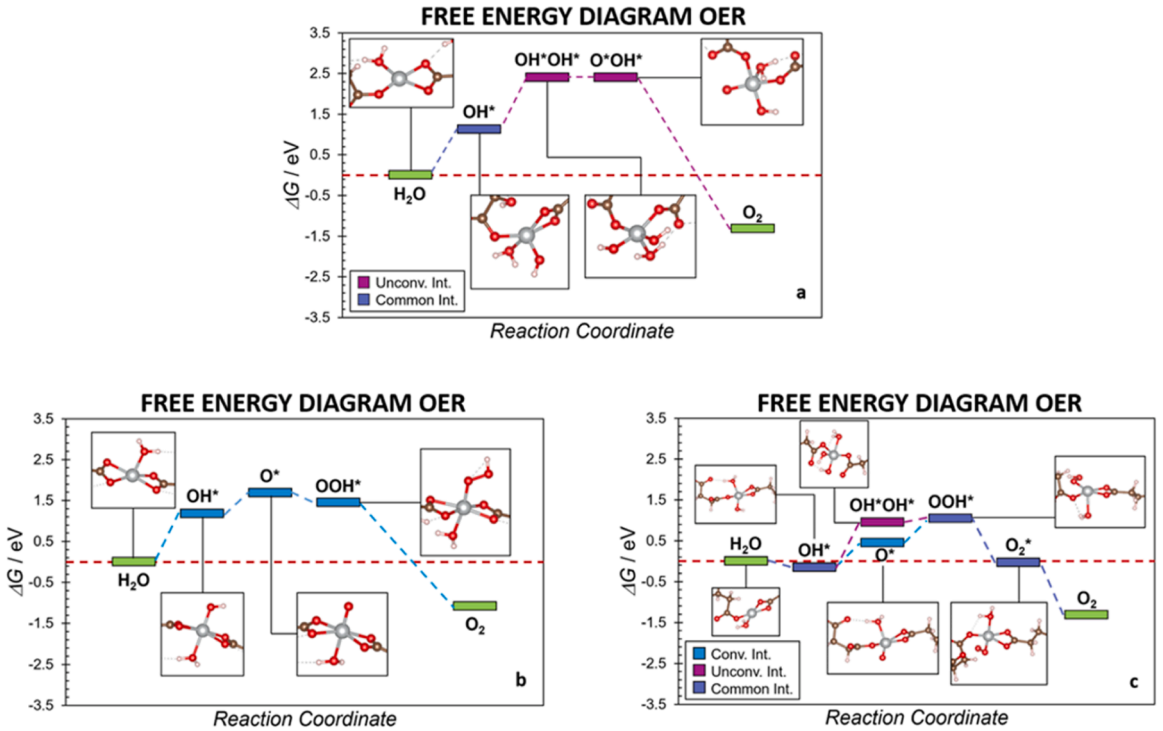

Fig. 11. Calculated OER Gibbs free energy profiles of a) NiSuc and b,c) NiTar samples. Panels a) and c) are for asymmetric coordination of Ni. Panel b) relies to the square planar coordination of Ni. All catalysts have as additional ligand one water molecule.

also considered, but the catalyst was unable to bind intermediates. Interestingly, as the number of water molecules increases, the OER intermediates becomes less stable due the increasing of the metal coordination by water molecules and the overpotential increases (indeed, coordination with two water molecules is not stable). Table 4 summarizes the calculated overpotentials.

Only the undercoordinated NiSuc is compatible with the experimental observation, according to the measured overpotential, 0.33 V (see Section 3.3). In particular, the calculated overpotential, $\eta = 0.46$ V, displays a very small deviation, 0.13 V only, which is within the accuracy of the method.

Moving to the NiTar catalyst, the OER profile of the most stable NiTar catalyst having a square planar configuration is consistent with the previous case, where the classical OH*, O*, OOH* path where before the release of O_2 a superoxo ($d_{OO} = 1.26$ Å) complex form [79] (see Fig. 10b). The calculated overpotential is 0.52 V. The same profile obtained by considering a water molecule coordinating the metal leads to an overpotential of 1.18 V (see Fig. 11b). The second possible NiTar configuration of the catalyst is rather unlikely as it is much less stable. If we look at the OER predicted activity, we see that the overpotential is 0.57 V, similar to the previous case (see Fig. 10d). The same catalyst with an extra ligand (water molecule) is predicted as less active, $\eta = 1.13$ V. Again, the presence of coordinating water molecules reduces the ability to bind OER intermediates, resulting into higher overpotential (see Fig. 11c). Among the two possible active structures, the second one is much less stable, and therefore it is unlikely to be the active phase. Therefore, in the case of NiTar the square planar coordinated Ni looks like the active phase. Another evidence of this can be extracted by comparing the measured Tafel slopes with the calculated Gibbs Free energies profile [80]. Indeed, the measured Tafel slopes (see Section 3.3) of NiTar is compatible with a OER mechanism with a weak OH* binding, which is exactly what found in the energy profile of the NiTar catalyst having a square planar coordination (see Fig. 10c)). On the other hand, the less symmetric active site strongly binds OH* (see Fig. 10d)). Moving to the NiSuc catalyst, the analysis of the energy profiles indicates that the model reconciling with the observed activity corresponds to the Ni atom coordinated asymmetrically by the succinate ligands. This result is further corroborated by the measured Tafel slopes that indicate that the OER process occurs via weak binding of OH*, the same result obtained by the numerical simulations (see Fig. 10b)). Eventually, NiSuc is expected to display an overpotential about 100 mV lower than NiTar, consistently with the experimental observation.

Table 4
Calculated overpotentials of NiSuc and NiTar catalysts.

NiSuc		NiTar	
SAC_square planar		SAC_square planar	
Water coordination	η [V]	Water coordination	η [V]
Dry	1.11	Dry	0.52
1 H_2O	–	1 H_2O	1.18
SAC_undercoordinated		SAC_undercoordinated	
Water coordination	η [V]	Water coordination	η [V]
Dry	0.44	Dry	0.57
1 H_2O	0.63	1 H_2O	1.13

4. Conclusions

Succinate and tartrate-based MOF nanostructures were successfully synthesized on SS mesh substrate by an optimized electrodeposition process carried out in mild conditions to prepare a free-standing porous electrode for OER in alkaline environment. Electrocatalytic activity of MOF-based electrodes was guaranteed by the presence of coordinated Ni.

Succinate-based electrodes reported the best performances, with a low Tafel slope value of 46 mV dec^{-1} assessed in flow-through cell configuration, close to that assessed for the benchmark materials for OER. These samples showed long-term stability and durable electrochemical activity, delivering 50 mA cm^{-2} for (at least) 100 h in 1 M KOH aqueous solution without degradation sign. Moreover, succinate-based MOF electrode also exhibited outstanding 100 h stability in very aggressive environment, i.e. 6 M aqueous KOH, typical of real industrial alkaline electrolyzers, delivering 50 mA cm^{-2} at an overpotential value of 260 mV. This performance can be rationalized taking into account the synergistic action of very active Ni with very stable succinate.

DFT calculations confirmed experimental results, assessing higher activity for Ni succinate-based electrocatalyst than Ni tartrate one. Moreover, highest activity was reported considering an asymmetrically coordinated Ni metal center without any water molecule as ligand for succinate-based electrocatalyst, indicating also that OER process occurs via weak binding of OH* species.

Declaration of competing interest

The authors declare that they have no known competing financial interests or personal relationships that could have appeared to influence the work reported in this paper.

Acknowledgments

AZ has received funding by European Social Fund (ESF)—Complementary Operational Programme (POC) 2014/2020 of Sicily. GDL has received funding through the PRIN project "UNDERSAC" (project code 2022LRPSTS) by the Italian Ministry for Universities and Research (MUR). GDL has received funding through the PRIN PNRR project "SACtoH2″ (project code P2022AZETB) by the Italian Ministry for Universities and Research (MUR), in the context of the National Recovery and Resilience Plan and co-financed by the Next Generation EU. GDL, CS, EI thank the support from CINECA for the access of supercomputing power via ISCRA B projects.

Supplementary materials

Supplementary material associated with this article can be found, in the online version, at doi:10.1016/j.electacta.2024.145416.

References

[1] https://sdgresources.relx.com/goal-7-affordable-and-clean-energy, (n.d.).
[2] International Renewable Energy Agency (IRENA), Green hydrogen cost reduction: scaling up electrolysers to meet the 1.5°C climate goal, Abu Dhabi, 2020.
[3] A.I. Osman, N. Mehta, A.M. Elgarahy, M. Hefny, A. Al-Hinai, A.H. Al-Muhtaseb, D. W. Rooney, Hydrogen production, storage, utilisation and environmental impacts: a review, Environ. Chem. Lett. 20 (2022) 153–188, https://doi.org/10.1007/s10311-021-01322-8.
[4] J.A. Luque-Urrutia, T. Ortiz-García, M. Solà, A. Poater, Green energy by hydrogen production from water splitting, water oxidation catalysis and acceptorless dehydrogenative coupling, Inorganics. (Basel) 11 (2023), https://doi.org/10.3390/inorganics11020088.
[5] D. Zhou, P. Li, W. Xu, S. Jawaid, J. Mohammed-Ibrahim, W. Liu, Y. Kuang, X. Sun, Recent advances in non-precious metal-based electrodes for alkaline water electrolysis, ChemNanoMat. 6 (2020) 336–355, https://doi.org/10.1002/cnma.202000010.
[6] C. Santoro, A. Lavacchi, P. Mustarelli, V. Di Noto, L. Elbaz, D.R. Dekel, F. Jaouen, What is next in anion-exchange membrane water electrolyzers? Bottlenecks, benefits, and future, ChemSusChem. 15 (2022) e202200027.
[7] T. Reier, M. Oezaslan, P. Strasser, Electrocatalytic oxygen evolution reaction (OER) on Ru, Ir, and pt catalysts: a comparative study of nanoparticles and bulk materials, ACS. Catal. 2 (2012) 1765–1772, https://doi.org/10.1021/CS3003098/.
[8] H. Sun, Z. Yan, F. Liu, W. Xu, F. Cheng, J. Chen, Self-supported transition-metal-based electrocatalysts for hydrogen and oxygen evolution, Adv. Mater. 32 (2020) 1806326, https://doi.org/10.1002/ADMA.201806326.
[9] Y. Luo, Z. Zhang, M. Chhowalla, B. Liu, Recent advances in design of electrocatalysts for high-current-density water splitting, Adv. Mater. 34 (2022), https://doi.org/10.1002/adma.202108133.
[10] A.W. Tricker, T.Y. Ertugrul, J.K. Lee, J.R. Shin, W. Choi, D.I. Kushner, G. Wang, J. Lang, I.V. Zenyuk, A.Z. Weber, X. Peng, Pathways toward efficient and durable anion exchange membrane water electrolyzers enabled by electro-active porous

transport layers, Adv. Energy Mater. (2023) 2303629, https://doi.org/10.1002/aenm.202303629.
[11] R. Wei, H.Y. Chi, X. Li, D. Lu, Y. Wan, C.W. Yang, Z. Lai, Aqueously cathodic deposition of ZIF-8 membranes for superior propylene/propane separation, Adv. Funct. Mater. 30 (2020), https://doi.org/10.1002/adfm.201907089.
[12] X. Zhang, K. Wan, P. Subramanian, M. Xu, J. Luo, J. Fransaer, Electrochemical deposition of metal-organic framework films and their applications, J. Mater. Chem. a Mater. 8 (2020) 7569–7587, https://doi.org/10.1039/d0ta00406e.
[13] K. Jayaramulu, M.Esclance Dmello, K. Kesavan, A. Schneemann, M. Otyepka, S. Kment, C. Narayana, S.B. Kalidindi, R.S. Varma, R. Zboril, R.A. Fischer, A multifunctional covalently linked graphene-MOF hybrid as an effective chemiresistive gas sensor, J. Mater. Chem. a Mater. 9 (2021) 17434–17441, https://doi.org/10.1039/d1ta03246a.
[14] B. He, Q. Zhang, Z. Pan, L. Li, C. Li, Y. Ling, Z. Wang, M. Chen, Z. Wang, Y. Yao, Q. Li, L. Sun, J. Wang, L. Wei, Freestanding metal-organic frameworks and their derivatives: an emerging platform for electrochemical energy storage and conversion, Chem. Rev. 122 (2022) 10087–10125, https://doi.org/10.1021/acs.chemrev.1c00978.
[15] Y. Zhou, R. Abazari, J. Chen, M. Tahir, A. Kumar, R.R. Ikreedeegh, E. Rani, H. Singh, A.M. Kirillov, Bimetallic metal–organic frameworks and MOF-derived composites: recent progress on electro- and photoelectrocatalytic applications, Coord. Chem. Rev. 451 (2022), https://doi.org/10.1016/j.ccr.2021.214264.
[16] H. Furukawa, K.E. Cordova, M. O'Keeffe, O.M. Yaghi, The chemistry and applications of metal-organic frameworks, Science 341 (2013) 1230444, https://doi.org/10.1126/science.1230444.
[17] H.F. Wang, L. Chen, H. Pang, S. Kaskel, Q. Xu, MOF-derived electrocatalysts for oxygen reduction, oxygen evolution and hydrogen evolution reactions, Chem. Soc. Rev. 49 (2020) 1414–1448, https://doi.org/10.1039/c9cs00906j.
[18] D. Li, H.Q. Xu, L. Jiao, H.L. Jiang, Metal-organic frameworks for catalysis: state of the art, challenges, and opportunities, EnergyChem. 1 (2019) 100005, https://doi.org/10.1016/J.ENCHEM.2019.100005.
[19] Y. Guo, C. Zhang, J. Zhang, K. Dastafkan, K. Wang, C. Zhao, Z. Shi, Metal-organic framework-derived bimetallic nife selenide electrocatalysts with multiple phases for efficient oxygen evolution reaction, ACS. Sustain. Chem. Eng. 9 (2021) 2047–2056, https://doi.org/10.1021/acssuschemeng.0c06969.
[20] F. Shahbazi Farahani, M.S. Rahmanifar, A. Noori, M.F. El-Kady, N. Hassani, M. Neek-Amal, R.B. Kaner, M.F. Mousavi, Trilayer metal-organic frameworks as multifunctional electrocatalysts for energy conversion and storage applications, J. Am. Chem. Soc. 144 (2022) 3411–3428, https://doi.org/10.1021/jacs.1c10963.
[21] H. Wu, W. Zheng, R. Zhu, M. Zhou, X. Ren, Y. Wang, C. Cheng, H. Zhou, S. Cao, Modulating coordination structures and metal environments of MOFs-Engineered electrocatalysts for water electrolysis, Chem. Eng. J. 452 (2023), https://doi.org/10.1016/j.cej.2022.139475.
[22] Y. Li, Z. Gao, H. Bao, B. Zhang, C. Wu, C. Huang, Z. Zhang, Y. Xie, H. Wang, Amorphous nickel-cobalt bimetal-organic framework nanosheets with crystalline motifs enable efficient oxygen evolution reaction: ligands hybridization engineering, J. Energy Chem. 53 (2021) 251–259, https://doi.org/10.1016/j.jechem.2020.05.002.
[23] Y. Xie, M. Liu, Y. Li, Z. Zhang, C. Wu, C. Huang, Z. Guo, H. Wang, Toward efficient cobalt-based oxygen evolution reaction: heteropolyatomic anion-inductive effect, Mater. Today Energy 24 (2022) 100922, https://doi.org/10.1016/j.mtener.2021.100922.
[24] N. Campagnol, T.R.C. Van Assche, M. Li, L. Stappers, M. Dinca, J.F.M. Denayer, K. Binnemans, D.E. De Vos, J. Fransaer, On the electrochemical deposition of metal-organic frameworks, J. Mater. Chem. a Mater. 4 (2016) 3914–3925, https://doi.org/10.1039/c5ta10782b.
[25] B. Zhang, P. Huang, J. Chen, X. Dang, Y. Hu, Y. Ai, D. Zheng, H. Chen, One-step controlled electrodeposition of iron-based binary metal organic nanocomposite, Appl. Surf. Sci. 504 (2020), https://doi.org/10.1016/j.apsusc.2019.144504.
[26] A.Mariella Babu, A. Varghese, Electrochemical deposition for metal organic frameworks: advanced energy, catalysis, sensing and separation applications, J. Electroanalyt. Chem. 937 (2023), https://doi.org/10.1016/j.jelechem.2023.117417.
[27] K.W. Jung, B.H. Choi, S.Y. Lee, K.H. Ahn, Y.J. Lee, Green synthesis of aluminum-based metal organic framework for the removal of azo dye Acid Black 1 from aqueous media, J. Ind. Eng. Chem. 67 (2018) 316–325, https://doi.org/10.1016/j.jiec.2018.07.003.
[28] N. Fajrin, I.R. Saragi, Y.K. Krisnandi, A. Zulys, Synthesis of metal organic framework (MOF) using lanthanum and yttrium metals with succinate acid ligand as adsorbent for cadmium(II) metal ion, in: AIP Conference Proceeding, American Institute of Physics Inc., 2020, https://doi.org/10.1063/5.0008318.
[29] D.A. Nurani, B.C.B. Butar, Y.K. Krisnandi, Synthesis and characterization of metal organic framework using succinic acid ligand with cobalt and iron metals as methylene blue dye adsorbent, in: IOP Conference Series: Materials Science and Engineering, IOP Publishing Ltd, 2020, https://doi.org/10.1088/1757-899X/902/1/012055.
[30] A. Sharma, M. Kumari, M. Tahir, S. Jain, S. Sharma, N. Kumar, An energy saving and water- based synthesis of Bi2O3@Fe-succinate MOF: a visible light mediated approach towards water decontamination, J. Mol. Liq. 386 (2023), https://doi.org/10.1016/j.molliq.2023.122429.
[31] A. Palčić, A. Puškarić, M. Mazaj, E. Žunkovič, N.Z. Logar, J. Bronić, Structural and degradation studies of a biocompatible Zn-L -tartrate metal-organic framework, J. Solid. State Chem. 225 (2015) 59–64, https://doi.org/10.1016/j.jssc.2014.11.028.
[32] U. Huizi-Rayo, X. Gastearena, A.M. Ortuño, J.M. Cuerva, A. Rodríguez-Diéguez, J. A. García, J. Ugalde, J.M. Seco, E.S. Sebastian, J. Cepeda, Influence of tartrate ligand coordination over luminescence properties of chiral lanthanide-based metal–organic frameworks, Nanomaterials 12 (2022), https://doi.org/10.3390/nano12223999.
[33] C. Jandl, G. Steinfeld, K. Li, P.K.C. Pang, C.L. Choi, C. Wang, P. Simoncic, I. D. Williams, Absolute structure determination of chiral zinc tartrate MOFs by 3D electron diffraction, Symmetry. (Basel) (2023) 15, https://doi.org/10.3390/sym15050983.
[34] G. Kresse, J. Hafner, Ab initio molecular dynamics for liquid metals, Phys. Rev. B 47 (1993) 558–561, https://doi.org/10.1103/PhysRevB.47.558.
[35] G. Kresse, J. Furthmüller, Efficiency of ab-initio total energy calculations for metals and semiconductors using a plane-wave basis set, Comput. Mater. Sci. 6 (1996) 15–50, https://doi.org/10.1016/0927-0256(96)00008-0.
[36] G. Kresse, J. Hafner, Ab initio molecular-dynamics simulation of the liquid-metal–amorphous-semiconductor transition in germanium, Phys. Rev. B 49 (1994) 14251–14269, https://doi.org/10.1103/PhysRevB.49.14251.
[37] J.P. Perdew, K. Burke, M. Ernzerhof, Generalized gradient approximation made simple, Phys. Rev. Lett. 77 (1996) 3865–3868, https://doi.org/10.1103/PhysRevLett.77.3865.
[38] P.E. Blöchl, Projector augmented-wave method, Phys. Rev. B 50 (1994) 17953–17979, https://doi.org/10.1103/PhysRevB.50.17953.
[39] G. Kresse, D. Joubert, From ultrasoft pseudopotentials to the projector augmented-wave method, Phys. Rev. B 59 (1999) 1758–1775, https://doi.org/10.1103/PhysRevB.59.1758.
[40] S. Grimme, J. Antony, S. Ehrlich, H. Krieg, A consistent and accurate ab initio parametrization of density functional dispersion correction (DFT-D) for the 94 elements H-Pu, J. Chem. Phys. 132 (2010) 154104, https://doi.org/10.1063/1.3382344.
[41] C. Adamo, V. Barone, Toward reliable density functional methods without adjustable parameters: the PBE0 model, J. Chem. Phys. 110 (1999) 6158–6170, https://doi.org/10.1063/1.478522.
[42] J.P. Perdew, M. Ernzerhof, K. Burke, Rationale for mixing exact exchange with density functional approximations, J. Chem. Phys. 105 (1996) 9982–9985, https://doi.org/10.1063/1.472933.
[43] I. Barlocco, L.A. Cipriano, G. Di Liberto, G. Pacchioni, Modeling hydrogen and oxygen evolution reactions on single atom catalysts with density functional theory: role of the functional, Adv. Theory. Simul. (2022) 2200513, https://doi.org/10.1002/adts.202200513.
[44] I. Barlocco, L.A. Cipriano, G. Di Liberto, G. Pacchioni, Modeling hydrogen and oxygen evolution reactions on single atom catalysts with density functional theory: role of the functional, Adv. Theory. Simul. 6 (2023), https://doi.org/10.1002/adts.202200513.
[45] C. Saetta, I. Barlocco, G. Di Liberto, G. Pacchioni, Key Ingredients for the screening of single atom catalysts for the hydrogen evolution reaction: the case of titanium nitride, Small. (2024), https://doi.org/10.1002/smll.202401058.
[46] G. Di Liberto, L. Giordano, G. Pacchioni, Predicting the stability of single-atom catalysts in electrochemical reactions, ACS. Catal. 14 (2024) 45–55, https://doi.org/10.1021/acscatal.3c04801.
[47] J.K. Nørskov, T. Bligaard, A. Logadottir, J.R. Kitchin, J.G. Chen, S. Pandelov, U. Stimming, Trends in the exchange current for hydrogen evolution, J. Electrochem. Soc. 152 (J23) (2005), https://doi.org/10.1149/1.1856988.
[48] J.K. Nørskov, T. Bligaard, J. Rossmeisl, C.H. Christensen, Towards the computational design of solid catalysts, Nat. Chem. 1 (2009) 37–46, https://doi.org/10.1038/nchem.121.
[49] M. Pourbaix, Atlas of Electrochemical Equilibria in Aqueous Solutions, Pergamon Press, Oxford, UK, 1966.
[50] G. Zhong, S. Xu, L. Liu, C.Z. Zheng, J. Dou, F. Wang, X. Fu, W. Liao, H. Wang, Effect of experimental operations on the limiting current density of oxygen reduction reaction evaluated by rotating-disk electrode, ChemElectroChem. 7 (2020) 1107–1114, https://doi.org/10.1002/celc.201902085.
[51] J. Wang, C.X. Zhao, J.N. Liu, D. Ren, B.Q. Li, J.Q. Huang, Q. Zhang, Quantitative kinetic analysis on oxygen reduction reaction: a perspective, Nano Mater. Sci. 3 (2021) 313–318, https://doi.org/10.1016/j.nanoms.2021.03.006.
[52] C. Fei, N. Ma, Q. Zhong, Y. Wang, M. Li, Oxygen-reduction-triggered cathodic electrodeposition of Mn-based metal-organic framework nanoflakes as oxygen evolution electrocatalysts, ACS. Appl. Nano Mater. 6 (2023) 20139–20148, https://doi.org/10.1021/acsanm.3c03913.
[53] J.T. Richardson, R. Scates, M.V. Twigg, X-ray diffraction study of nickel oxide reduction by hydrogen, Appl. Catal. A Gen. 246 (2003) 137–150, https://doi.org/10.1016/S0926-860X(02)00669-5.
[54] A.Y. Faid, A.O. Barnett, F. Seland, S. Sunde, Ni/NiO nanosheets for alkaline hydrogen evolution reaction: in situ electrochemical-Raman study, Electrochim. Acta 361 (2020), https://doi.org/10.1016/j.electacta.2020.137040.
[55] S. Krishnan, C.J. Raj, R. Robert, A. Ramanand, S. Jerome Das, Growth and characterization of succinic acid single crystals, Cryst. Res. Technol. 42 (2007) 1087–1090, https://doi.org/10.1002/crat.200710981.
[56] D. Bieńko, M. Malik-Gajewska, P. Walencik, M. Kaj, W. Zierkiewicz, G. Murtaza, T. Ruffer, S. Ahmad, IR and Raman spectroscopic analysis, DFT modeling, and magnetic properties of a nickel(II) complex, [Ni(succ)(H2O)4]n, J. Coord. Chem. 72 (2019) 2215–2232, https://doi.org/10.1080/00958972.2019.1650351.
[57] Y. Hai, L. Liu, Y. Gong, Iron coordination polymer, Fe(oxalate)(H2O)2 nanorods grown on nickel foam via one-step electrodeposition as an efficient electrocatalyst for oxygen evolution reaction, Inorg. Chem. 60 (2021) 5140–5152, https://doi.org/10.1021/acs.inorgchem.1c00170.
[58] S.A. Martin Britto Dhas, M. Suresh, G. Bhagavannarayana, S. Natarajan, Growth and characterization of L-Tartaric acid, an NLO material, J. Cryst. Growth 309 (2007) 48–52, https://doi.org/10.1016/j.jcrysgro.2007.09.008.

[59] G. Tranchida, M. Clesi, F. Di Franco, F. Di Quarto, M. Santamaria, Electronic properties and corrosion resistance of passive films on austenitic and duplex stainless steels, Electrochim. Acta 273 (2018) 412–423, https://doi.org/10.1016/j.electacta.2018.04.058.
[60] J. Luo, J.-H. Im, M.T. Mayer, M. Schreier, M.K. Nazeeruddin, N.-G. Park, S. D. Tilley, H.J. Fan, M. Graetzel, Water photolysis at 12.3% efficiency via perovskite photovoltaics and Earth-abundant catalysts, Science 345 (2014) 1593–1596.
[61] N.T. Suen, S.F. Hung, Q. Quan, N. Zhang, Y.J. Xu, H.M. Chen, Electrocatalysis for the oxygen evolution reaction: recent development and future perspectives, Chem. Soc. Rev. 46 (2017) 337–365, https://doi.org/10.1039/c6cs00328a.
[62] G. Li, L. Anderson, Y. Chen, M. Pan, P.Y. Abel Chuang, New insights into evaluating catalyst activity and stability for oxygen evolution reactions in alkaline media, Sustain. Energy Fuels. 2 (2018) 237–251, https://doi.org/10.1039/c7se00337d.
[63] C.P. Wang, Y.X. Lin, L. Cui, J. Zhu, X.H. Bu, 2D metal–organic frameworks as competent electrocatalysts for water splitting, Small. 19 (2023), https://doi.org/10.1002/smll.202207342.
[64] O. van der Heijden, S. Park, J.J.J. Eggebeen, M.T.M. Koper, Non-kinetic effects convolute activity and Tafel analysis for the alkaline oxygen evolution reaction on NiFeOOH Electrocatalysts, Angew. Chem. - Int. Ed. 62 (2023), https://doi.org/10.1002/anie.202216477.
[65] E. Tsuji, A. Imanishi, K.I. Fukui, Y. Nakato, Electrocatalytic activity of amorphous RuO2 electrode for oxygen evolution in an aqueous solution, Electrochim. Acta 56 (2011) 2009–2016, https://doi.org/10.1016/j.electacta.2010.11.062.
[66] Y. Lee, J. Suntivich, K.J. May, E.E. Perry, Y. Shao-Horn, Synthesis and activities of rutile IrO2 and RuO2 nanoparticles for oxygen evolution in acid and alkaline solutions, J. Phys. Chem. Lett. 3 (2012) 399–404, https://doi.org/10.1021/jz2016507.
[67] L. Wang, Y. Wu, R. Cao, L. Ren, M. Chen, X. Feng, J. Zhou, B. Wang, Fe/Ni metal-organic frameworks and their binder-free thin films for efficient oxygen evolution with low overpotential, ACS. Appl. Mater. Interfaces. 8 (2016) 16736–16743, https://doi.org/10.1021/acsami.6b05375.
[68] B. Hirschorn, M.E. Orazem, B. Tribollet, V. Vivier, I. Frateur, M. Musiani, Determination of effective capacitance and film thickness from constant-phase-element parameters, Electrochim. Acta 55 (2010) 6218–6227, https://doi.org/10.1016/j.electacta.2009.10.065.
[69] D.M. Morales, M. Risch, Seven steps to reliable cyclic voltammetry measurements for the determination of double layer capacitance, J. Phys. Energy 3 (2021), https://doi.org/10.1088/2515-7655/abee33.
[70] A. Zaffora, F. Di Franco, D. Pupillo, B. Seminara, G. Tranchida, M. Santamaria, Highly active and stable NiCuMo electrocatalyst supported on 304 stainless steel porous transport layer for hydrogen evolution in alkaline water electrolyzer, Adv. Sustain. Syst. 7 (2023), https://doi.org/10.1002/adsu.202200486.
[71] F. Zeng, C. Mebrahtu, L. Liao, A.K. Beine, R. Palkovits, Stability and deactivation of OER electrocatalysts: a review, J. Energy Chem. 69 (2022) 301–329, https://doi.org/10.1016/j.jechem.2022.01.025.
[72] L. Xiao, Z. Wang, J. Guan, 2D MOFs and their derivatives for electrocatalytic applications: recent advances and new challenges, Coord. Chem. Rev. 472 (2022), https://doi.org/10.1016/j.ccr.2022.214777.
[73] A.J. Bard, L.R. Faulkner, Electrochemical Methods. Fundamentals and Applications, 2nd ed., John Wiley & Sons, 2001.
[74] I. Barlocco, L.A. Cipriano, G. Di Liberto, G. Pacchioni, Does the oxygen evolution reaction follow the classical OH*, O*, OOH* path on single atom catalysts? J. Catal. 417 (2023) 351–359, https://doi.org/10.1016/j.jcat.2022.12.014.
[75] G. Di Liberto, G. Pacchioni, Modeling single-atom catalysis, Adv. Mater. 35 (2023), https://doi.org/10.1002/adma.202307150.
[76] L. Zhong, S. Li, Unconventional oxygen reduction reaction mechanism and scaling relation on single-atom catalysts, ACS. Catal. 10 (2020) 4313–4318, https://doi.org/10.1021/acscatal.0c00815.
[77] D. Misra, G. Di Liberto, G. Pacchioni, CO2 electroreduction on single atom catalysts: is water just a solvent? J. Catal. 422 (2023) 1–11, https://doi.org/10.1016/j.jcat.2023.04.002.
[78] D. Misra, G. Di Liberto, G. Pacchioni, CO2 electroreduction on single atom catalysts: the role of the DFT functional, Phys. Chem. Chem. Phys. 26 (2024) 10746–10756, https://doi.org/10.1039/d4cp00175c.
[79] L.A. Cipriano, G. Di Liberto, G. Pacchioni, Superoxo and peroxo complexes on single-atom catalysts: impact on the oxygen evolution reaction, ACS. Catal. 12 (2022) 11682–11691, https://doi.org/10.1021/acscatal.2c03020.
[80] D. Antipin, M. Risch, Calculation of the Tafel slope and reaction order of the oxygen evolution reaction between pH 12 and pH 14 for the adsorbate mechanism, Electrochem. Sci. Adv. 3 (2023), https://doi.org/10.1002/elsa.202100213.